



1 **Composited analyses of the chemical and physical characteristics of co-**
2 **polluted days by ozone and PM_{2.5} over 2013-2020 in the Beijing–Tianjin–Hebei**
3 **region**

4
5 Huibin Dai¹, Hong Liao^{1*}, Ke Li¹, Xu Yue¹, Yang Yang¹, Jia Zhu¹, Jianbing Jin¹,
6 Baojie Li¹

7
8 ¹Jiangsu Key Laboratory of Atmospheric Environment Monitoring and Pollution
9 Control, Jiangsu Collaborative Innovation Center of Atmospheric Environment and
10 Equipment Technology, School of Environmental Science and Engineering, Nanjing
11 University of Information Science & Technology, Nanjing 210044, China

12
13 *Correspondence to: Hong Liao (hongliao@nuist.edu.cn)

14



15 **Abstract.**

16 The co-polluted days by ozone (O_3) and $PM_{2.5}$ (particulate matter with an
17 aerodynamic equivalent diameter of $2.5 \mu m$ or less) ($O_3&PM_{2.5}PD$) were frequently
18 observed in the Beijing–Tianjin–Hebei (BTH) region in warm seasons (April–October)
19 of 2013–2020. We applied the 3-D global chemical transport model (GEOS-Chem) to
20 investigate the chemical and physical characteristics of $O_3&PM_{2.5}PD$ by composited
21 analyses of such days that were captured by both the observations and the model. Model
22 results showed that, when $O_3&PM_{2.5}PD$ occurred, the concentrations of hydroxyl
23 radical and total oxidant, sulfur oxidation ratio, and nitrogen oxidation ratio were all
24 high, and the concentrations of sulfate at the surface were the highest among all aerosol
25 species. We also found unique features in vertical distributions of aerosols during
26 $O_3&PM_{2.5}PD$; concentrations of $PM_{2.5}$ decreased with altitude near the surface but
27 remained stable at 975–819 hPa. Process analyses showed that secondary aerosols
28 (nitrate, ammonium and sulfate) had strong chemical productions at 913–819 hPa,
29 which were then transported downward, resulting in the quite uniform vertical profiles
30 at 975–819 hPa in $O_3&PM_{2.5}PD$. The weather patterns for $O_3&PM_{2.5}PD$ were
31 characterized by a high pressure ridge of the Western Pacific Subtropical High at 850
32 hPa. The strong southerlies at 850 hPa brought moist air from the south, resulting in a
33 high RH and hence the strong chemical productions around this layer in $O_3&PM_{2.5}PD$.
34 The physical and chemical characteristics of $O_3&PM_{2.5}PD$ are quite different from
35 those of polluted days by either O_3 alone or $PM_{2.5}$ alone, which have important
36 implications for air quality management.

37

38 **Keywords:** Co-occurrence, Ozone and $PM_{2.5}$, Pollution, Meteorological parameters.

39



40 1. Introduction

41 Surface ozone (O_3) and $PM_{2.5}$ (particulate matter with an aerodynamic equivalent
42 diameter of 2.5 micrometers or less) are important air pollutants in the atmosphere that
43 have harmful effects on public health (Gao and Ji, 2018; Jiang et al., 2019), ecosystems
44 (Ren et al., 2011; Yue et al., 2017), and crops (Wang et al., 2005; Wang et al., 2007).
45 Surface O_3 is a secondary pollutant produced by photochemical oxidation of volatile
46 organic compounds (VOCs) and nitrogen oxides ($NO_x \equiv NO + NO_2$) in the presence of
47 intense ultraviolet light, and the major $PM_{2.5}$ components (nitrate (NO_3^-), ammonium
48 (NH_4^+), sulfate (SO_4^{2-}), black carbon (BC), organic carbon (OC)) are caused by
49 anthropogenic emissions of aerosols and aerosol precursors. Although surface O_3 and
50 $PM_{2.5}$ have different formation mechanisms, they are coupled through the common
51 precursors (NO_x and VOCs) and photochemical reactions (Chu et al., 2020). Since 2013,
52 stringent clean air actions have been implemented to improve air quality in China (State
53 Council of the People's Republic of China, 2013, 2018). However, O_3 concentrations
54 increased unexpectedly, while $PM_{2.5}$ concentrations decreased drastically in the past
55 years (Li et al., 2019). The co-polluted days by O_3 and $PM_{2.5}$ (concentrations of both
56 O_3 and $PM_{2.5}$ exceed the national air quality standards on the same day, hereafter
57 referred to as O_3 & $PM_{2.5}$ PD) were also reported (Dai et al., 2019). Therefore, it is
58 fundamental to examine the chemical and physical characteristics of O_3 & $PM_{2.5}$ PD.

59 The Beijing–Tianjin–Hebei (BTH) region is the most populated region in northern
60 China. In the past few years, concentrations of O_3 and $PM_{2.5}$ in the BTH were among
61 the highest in China. The Observations from China National Environmental Monitoring
62 Center (CNEMC) showed that the mean and maximum MDA8 (daily maximum 8-h
63 average) O_3 in North China in summer of 2019 were 83 ppb and 129 ppb, respectively,
64 and the summer mean MDA8 O_3 increased with a trend of 3.3 ppb a^{-1} over 2013–2019



65 (Li et al., 2020). Gong et al. (2020) reported that O₃ polluted days (i.e., MDA8 O₃
66 concentration exceeds 80 ppb) in May-July in the BTH increased from 35 days in the
67 year of 2014 to 56 days in 2018. As for observed PM_{2.5}, the concentration averaged
68 over BTH had a decreasing trend of 10 μg m⁻³ yr⁻¹ over 2013-2019, and the mean value
69 was 79 ± 17 μg m⁻³ over these years (Li et al., 2020). BTH also had the highest
70 frequency and intensity of severe haze pollution days (i.e., days with daily mean PM_{2.5}
71 concentration exceeding 150 μg m⁻³) in China from 2013 to 2017, with an observed
72 mean frequency of 21.2 d yr⁻¹ and an observed mean intensity of 231.6 μg m⁻³ (Dang
73 and Liao, 2019).

74 The interactions between O₃ and PM_{2.5} have been reported in previous studies.
75 Zhu et al. (2019) examined the spatial-temporal characteristics of the correlations
76 between observed O₃ and PM_{2.5} at 1497 sites in China for 2016 and found that O₃-
77 PM_{2.5} had the highest positive correlations (correlation coefficients > +0.7) in July in
78 southern China and the largest negative correlations (r values < -0.5) during January in
79 northern China. Li et al. (2019) used the GEOS-Chem model to analyze the O₃-PM_{2.5}
80 relationship in northern China and found that O₃ production was suppressed under high
81 PM_{2.5} conditions (PM_{2.5} concentrations > 60 μg m⁻³) because of the reactive uptake of
82 hydrogen oxide radicals (HO_x) by aerosol particles. Chu et al. (2020) analyzed the
83 observed daily PM_{2.5} and O₃ concentrations in 114 cities in China during years of 2013-
84 2018 and found that the correlations between O₃ and PM_{2.5} tended to change from
85 negative in 2013 to positive in 2018 in China as air quality improved.

86 Few previous studies have examined the co-occurrence of O₃ and PM_{2.5} pollution
87 (MDA8 O₃ > 80 ppb and PM_{2.5} > 75 μg m⁻³). Zong et al. (2021) used the obliquely
88 rotated principal component analysis in the T-mode (T-PCA) method to identify the
89 synoptic weather pattern associated with O₃&PM_{2.5}PD in eastern China during



90 summer of 2015–2018, and found that O_3 & $PM_{2.5}PD$ were associated with a stable
91 western Pacific subtropical high ridge, which brought warm and moist air flow from
92 the East China Sea to the eastern China to promote hygroscopic growth of fine
93 particulate matter in BTH and northern YRD. Dai et al. (2021) analyzed O_3 & $PM_{2.5}PD$
94 in the YRD for April–October of 2013–2019 by using observations and reported that
95 the co-polluted days occurred mainly in April (29.6% of co-polluted days occurred in
96 April), May (23.0%), June (19.5%), and October (10.8%) under meteorological
97 conditions of higher relative humidity, higher surface air temperature, and lower wind
98 speed relative to the days with O_3 pollution alone. Qin et al. (2021) investigated
99 O_3 & $PM_{2.5}PD$ by using the hourly observed concentrations of water-soluble ions, OC,
100 and elemental carbon (EC) in 2019 in cities of Nanjing and Changzhou. They found
101 that inorganic aerosols mainly existed as NH_4NO_3 and the correlation coefficients
102 between the secondary components NO_3^- , NH_4^+ , and SO_4^{2-} were relatively high during
103 O_3 & $PM_{2.5}PD$ in 2019, indicating a significant formation of secondary inorganic
104 aerosols. Although these studies have discussed the meteorological conditions and
105 some chemical characteristics of O_3 & $PM_{2.5}PD$, the understanding of O_3 & $PM_{2.5}PD$
106 was quite limited because of the limited observations of chemical species involved.

107 In this work, we take advantage of the comprehensive chemical mechanism of
108 the global chemical transport model to have better understanding of O_3 & $PM_{2.5}PD$. We
109 apply the 3-D global chemical transport model (GEOS-Chem) to simulate
110 O_3 & $PM_{2.5}PD$ in BTH in years of 2013–2020, and investigate the chemical and
111 physical characteristics of O_3 & $PM_{2.5}PD$ by composited analyses of such days that are
112 captured by both the observations and the model. The objectives of this study are: 1)
113 to examine the underlying chemical mechanisms for O_3 & $PM_{2.5}PD$ in BTH for warm
114 seasons (April–October) of 2013–2020 by comparing O_3 & $PM_{2.5}PD$ with polluted days



115 by O₃ alone or by PM_{2.5} alone, and 2) to identify the weather patterns that are
116 associated with O₃&PM_{2.5}PD in BTH. The observations, the reanalyzed
117 meteorological data, the GEOS-Chem model, and the process analysis are described
118 in Section 2. The observed O₃&PM_{2.5}PD are presented in Section 3.1. The evaluation
119 of simulated concentrations of O₃ and PM_{2.5} as well as the simulated pollution days by
120 O₃ and/or PM_{2.5} are shown in Section 3.2. The underlying mechanisms of
121 O₃&PM_{2.5}PD are shown in Section 3.3. In Section 3.4, the meteorological conditions
122 for the co-occurrence of O₃ and PM_{2.5} pollution are investigated. The conclusions are
123 presented in Section 4.

124

125 **2. Methods**

126 **2.1 Observed O₃ and PM_{2.5} concentrations**

127 Hourly concentrations of PM_{2.5} and O₃ in China over the years of 2013-2020
128 were taken from the public website of CNEMC (<https://air.cnemc.cn:18007/>,
129 CNEMC, 2022). To ensure data quality, the daily mean PM_{2.5} concentration was
130 calculated when there were valid data for more than 20 h during that day and the
131 MDA8 O₃ concentration was calculated when there were valid data for at least 6 h for
132 each 8 h. For the calculation of monthly and annual mean concentrations, the number
133 of days with valid concentrations had to be more than 15 in each month. The spatial
134 distribution of the 79 valid sites within BTH (37-41°N, 114-118°E, the black
135 rectangle) is shown in Fig. 1. For model evaluation, the observed concentrations were
136 averaged over sites within each of the 0.5° latitude × 0.625° longitude MERRA-2
137 grid cell. There are 18 model grids in BTH. Note that the observed O₃ concentrations
138 from this network have a unit of μg m⁻³. For the consistency of observed and
139 simulated O₃ concentrations, 1 μg m⁻³ of O₃ is approximately 0.5 ppb under the



140 conditions of 298 K and 1013 hPa. The observed O₃ concentrations reported by the
141 CNEMC were under standard conditions of 273 K and 1013 hPa before 31 August
142 2018 and were under standard conditions of 298 K and 1013 hPa afterwards
143 (http://www.mee.gov.cn/xxgk2018/xxgk/xxgk01/201808/t20180815_629602.html),
144 which were accounted for as O₃ concentrations were converted to ppb.

145 According to the National Ambient Air Quality Standard of China (GB3095-
146 2012), O₃ (PM_{2.5}) concentration exceeds the national air quality standard if the MDA8
147 O₃ (daily mean PM_{2.5}) concentration is higher than 160 μg m⁻³ (75 μg m⁻³). In this
148 study, we define O₃ polluted days (hereafter called ‘O₃PD’) for days with MDA8 O₃
149 concentration > 160 μg m⁻³, PM_{2.5} polluted days (hereafter called ‘PM_{2.5}PD’) with
150 daily mean PM_{2.5} concentration > 75 μg m⁻³, and the co-pollution days by O₃ and
151 PM_{2.5} (O₃&PM_{2.5}PD) with daily MDA8 O₃ concentration > 160 μg m⁻³ as well as the
152 daily mean PM_{2.5} concentration > 75 μg m⁻³.

153

154 2.2 Reanalyzed meteorological fields

155 Meteorological fields were obtained from the Version 2 of Modern Era
156 Retrospective-analysis for Research and Application (MERRA2), which were
157 generated by the NASA Global Modeling and Assimilation Office (GMAO). The
158 MERRA2 data have a horizontal resolution of 0.5° latitude × 0.625° longitude and
159 72 vertical layers (Molod et al., 2015). To analyze the meteorological conditions for
160 O₃&PM_{2.5}PD, vertical pressure velocity (OMEGA), planetary boundary layer height
161 (PBLH), temperature (T), relative humidity (RH), surface incoming shortwave flux
162 (SWGDN) are used. Note that the temporal resolution for PBLH, T, and SWGDN is
163 1h, and that for OMEGA and RH is 3h. Daily mean geopotential heights at 850 and
164 500 hPa from the National Center for Environmental Prediction (NCEP) and National



165 Center for Atmospheric Research (NCAR) global reanalysis with a resolution of 2.5°
166 latitude by 2.5° longitude are also utilized in this study.

167

168 **2.3 Observed aerosol optical depth**

169 We obtained the version 3 datasets of observed daily aerosol optical depth
170 (AOD) of level 2 (improved cloud screened and quality-assured) from Aerosol
171 Robotic Network (AERONET, https://aeronet.gsfc.nasa.gov/new_web/index.html)
172 established by NASA and LOA-PHOTONS (Giles et al., 2019). Three sites in the
173 BTH region have observations available over 2013-2020, including Beijing (39.97°N,
174 116.38°E), Beijing-CAMS (39.93°N, 116.31°E), and Xianghe (39.75°N, 116.96°E).
175 The AOD values at 440 nm and 675 nm at these three sites are analyzed in this study.

176

177 **2.4 GEOS-Chem model**

178 We simulated O₃ and PM_{2.5} using the nested version of the 3-D global chemical
179 transport model (GEOS-Chem, version 11-01) driven by the MERRA2
180 meteorological data. The nested domain was set over Asia (60°-150°E, 11°S-55°N)
181 with a horizontal resolution of 0.5° latitude × 0.625° longitude, and the chemical
182 boundary conditions were provided by the global GEOS-Chem simulation with 2.5°
183 latitude × 2.5° longitude horizontal resolution.

184 The GEOS-Chem model includes fully coupled O₃-NO_x-hydrocarbon and
185 aerosol chemistry mechanism (Bey et al., 2001; Pye et al., 2009) to simulate aerosols
186 including SO₄²⁻ (Park et al., 2004), NO₃⁻ (Pye et al., 2009), NH₄⁺, BC and OC (Park
187 et al., 2003), mineral dust (Fairlie et al., 2007), and sea salt (Alexander et al., 2005) as
188 well as the gas-phase pollutants such as NO_x and O₃. Over the Asian domain, the



189 anthropogenic emissions of OC, BC, carbon monoxide (CO), sulfur dioxide (SO₂),
190 NO_x, ammonia (NH₃), and VOCs were obtained from the Multi-resolution Emission
191 Inventory for China (MEIC), which includes emissions from industry, power,
192 residential and transportation sectors for years of 2014-2017 (Li et al., 2017; Zheng et
193 al., 2018), 2019 and 2020 (Zheng et al., 2021). Emissions in 2018 were obtained by
194 the interpolation of those in 2017 and 2019 for each grid due to the lack of publicly
195 accessible emission inventories for that year. The biogenic emissions in GEOS-Chem
196 are simulated using MEGAN v2.1 (Guenther et al., 2012).

197 The hourly O₃ and PM_{2.5} concentrations for the years of 2013-2020 were
198 simulated by the GEOS-Chem model which were driven by MERRA-2
199 meteorological fields. The model was spinned up for 6 months before the integration
200 over the studied time period.

201

202 **2.5 Process analysis**

203 Process analysis (PA) was applied to identify the relative importance of
204 atmospheric processes in O₃&PM_{2.5}PD. PA has been widely used in previous studies
205 to examine the key processes contributing to air pollution episodes (Gonçalves et al.,
206 2009; Dang and Liao, 2019; Gong and Liao, 2019) as well as the interannual and
207 decadal variations of air pollutants (Mu and Liao, 2014; Lou et al., 2015). Five major
208 processes that influence O₃ and PM_{2.5} concentrations were diagnosed at every time
209 step, including net chemical production, dry deposition, horizontal advection, vertical
210 advection, and diffusion, for the regional pollution days (days with more than half of
211 the sites in BTH experiencing pollutions). We carried out PA for O₃SPD (exclude
212 O₃&PM_{2.5}PD from O₃PD), PM_{2.5}SPD (exclude O₃&PM_{2.5}PD from PM_{2.5}PD), and
213 O₃&PM_{2.5}PD over BTH.



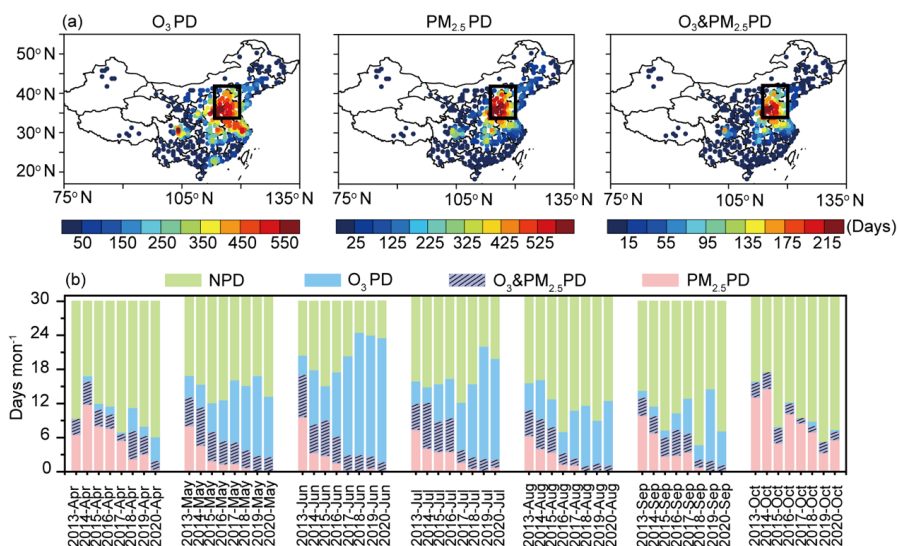
214

215 **3. Results**

216 **3.1 Observed polluted days by O₃ and PM_{2.5}**

217 Figure 1a shows the spatial distributions of observed numbers of O₃PD,
218 PM_{2.5}PD, and O₃&PM_{2.5}PD summed over the warm seasons (April-October) of 2013-
219 2020. The spatial distributions of polluted days in each year are shown in Fig. S1. The
220 numbers of O₃PD, PM_{2.5}PD, and O₃&PM_{2.5}PD were high in BTH, which were,
221 respectively, 524.3 344.6, and 128.1 days from observations, as the values were
222 averaged over all sites in BTH. The high numbers of O₃PD, PM_{2.5}PD, and
223 O₃&PM_{2.5}PD in BTH were associated with the highest anthropogenic emissions (NO_x
224 and NMVOCs) in this region (Dang et al., 2021).

225 Figure 1b shows the numbers of days averaged over all sites in BTH for non-
226 polluted days (NPD, MDA8 O₃ < 80 ppb and PM_{2.5} < 75 µg m⁻³), O₃PD,
227 O₃&PM_{2.5}PD, and PM_{2.5}PD in each month of warm seasons from 2013 to 2020. O₃PD
228 and O₃&PM_{2.5}PD mainly occurred in May, June, and July, while PM_{2.5}PD mainly
229 appeared in April and October. The monthly numbers of O₃&PM_{2.5}PD (PM_{2.5}PD)
230 declined from 2013 to 2020, with the fastest drop in June, from 7.5 (17.1) days in
231 June 2013 to 1.8 (1.8) days in June 2020. On the contrary, the numbers of O₃PD kept
232 increasing, especially in June, from 10.9 days in June 2013 to 23.6 days in June 2020.
233 The reductions in O₃&PM_{2.5}PD were associated with the large reductions in PM_{2.5}
234 since the implementation of the Clean Air Action in 2013.



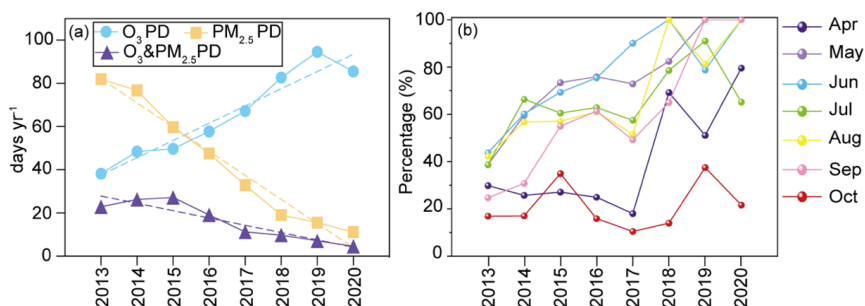
235

236 **Figure 1.** (a) Spatial distributions of observed numbers of O₃PD, PM_{2.5}PD, and
 237 O₃&PM_{2.5}PD summed over April-October of 2013-2020. The solid black rectangle
 238 indicates the BTH region. (b) The observed numbers of NPD (non-polluted days,
 239 green), O₃PD (blue + purple with slashes), O₃&PM_{2.5}PD (purple with slashes), and
 240 PM_{2.5}PD (pink + purple with slashes) averaged over all sites in BTH from April to
 241 October in 2013 to 2020.

242 Figure 2a shows the linear trends of observed O₃PD, PM_{2.5}PD, and O₃&PM_{2.5}PD
 243 in warm seasons of 2013-2020 averaged over the BTH. O₃PD showed an upward
 244 trend of 7.9 days yr⁻¹ from 2013 to 2020. However, the numbers of PM_{2.5}PD and
 245 O₃&PM_{2.5}PD decreased over 2013-2020, with linear trends of -11.2 and -3.4 days yr⁻¹,
 246 respectively. Figure 2b shows the changes in percentage of O₃&PM_{2.5}PD in PM_{2.5}PD
 247 from 2013 to 2020 for each month. It should be noted that, when PM_{2.5}PD occurred,
 248 the proportions of O₃&PM_{2.5}PD had an upward trend from 2013 to 2020. In May,
 249 June, August, and September of 2020, the proportions of O₃&PM_{2.5}PD in PM_{2.5}PD
 250 reached 100%, indicating that PM_{2.5} pollution was accompanied by O₃ pollution in



251 recent years.



252

253 **Figure 2.** (a) The trends of observed O₃PD, PM_{2.5}PD, and O₃&PM_{2.5}PD in warm
254 seasons from 2013 to 2020 averaged over all sites in BTH. The blue, yellow and purple
255 solid lines (dashed lines) represent the numbers (liner trend) of O₃PD, PM_{2.5}PD, and
256 O₃&PM_{2.5}PD, respectively. (b) The percentage of O₃&PM_{2.5}PD in PM_{2.5}PD for April
257 to October in 2013 to 2020. The polluted days were averaged over all sites in BTH.

258

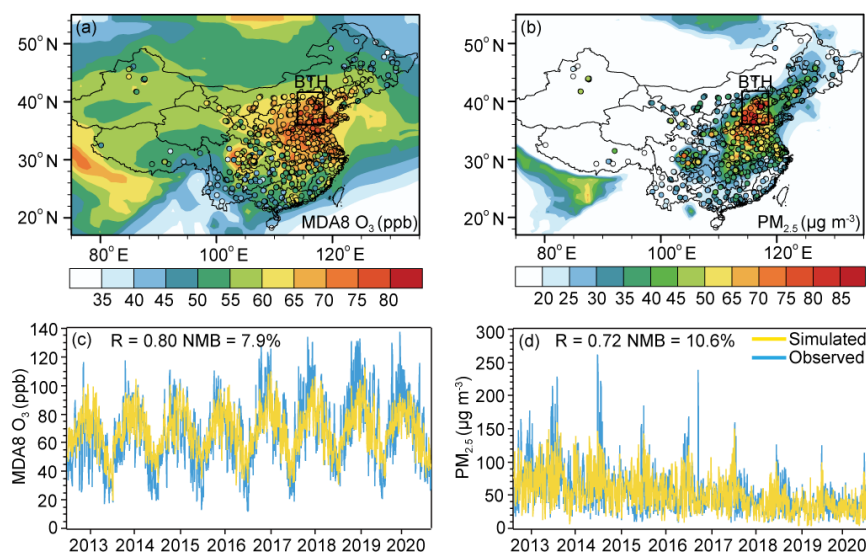
259 3.2 Simulated polluted days and model evaluation

260 3.2.1 Simulated surface-layer MDA8 O₃ and PM_{2.5} concentrations

261 Figures 3a and 3b show, respectively, the spatial distributions of simulated and
262 observed surface-layer concentrations of MDA8 O₃ and PM_{2.5} in China, as the
263 concentrations are averaged over the warm seasons (April-October) of 2013-2020.
264 The concentrations of MDA8 O₃ and PM_{2.5} were both high in BTH. Averaged over
265 BTH and the studied time period, the observed concentrations of MDA8 O₃ and PM_{2.5}
266 were 58.1 ppb and 60.3 $\mu\text{g m}^{-3}$, respectively, while the simulated values were 68.0 ppb
267 and 61.1 $\mu\text{g m}^{-3}$, respectively. Figures 3c and 3d compare the time series of observed
268 and simulated daily MDA8 O₃ and PM_{2.5} concentrations averaged over the BTH. The
269 simulated daily concentrations of MDA8 O₃ (PM_{2.5}) in eight warm seasons have a
270 normalized mean bias (NMB) of 7.9% (10.6%). The model generally captures the
271 daily variations (peaks and troughs) in the observed MDA8 O₃ and PM_{2.5}



272 concentrations, with R values of 0.80 and 0.72, respectively.



273

274 **Figure 3.** Spatial distributions of simulated (shades) and observed (CNEMC, dots)
275 surface-layer concentrations of (a) MDA8 O₃ (ppb) and (b) PM_{2.5} (µg m⁻³) averaged
276 over the eight warm seasons (April to October, 2013–2020). The solid black rectangle
277 in (a) and (b) indicates the BTH region. Simulated and observed daily concentrations
278 of surface-layer (c) MDA8 O₃ and (d) PM_{2.5} averaged over BTH. The correlation
279 coefficient (R) and normalized mean bias (NMB) are also shown for (c) and (d).

280
$$\text{NMB} = \left(\frac{\sum_{i=1}^N (M_i - O_i)}{\sum_{i=1}^N (O_i)} \right) \times 100\%$$
, where O_i and M_i are the observed and
281 simulated concentrations, respectively, i refers to the i^{th} day, and N is the total number
282 of days.

283 3.2.2 Simulated O₃PD, PM_{2.5}PD, and O₃&PM_{2.5}PD

284 Figure S2 shows the capability of the model in capturing the polluted days.
285 Although the GEOS-Chem model well reproduces the spatial distributions of observed
286 MDA8 O₃ and PM_{2.5} concentrations, it underestimates the numbers of O₃PD, PM_{2.5}PD,
287 and O₃&PM_{2.5}PD because of the model's deficiency in capturing the peak



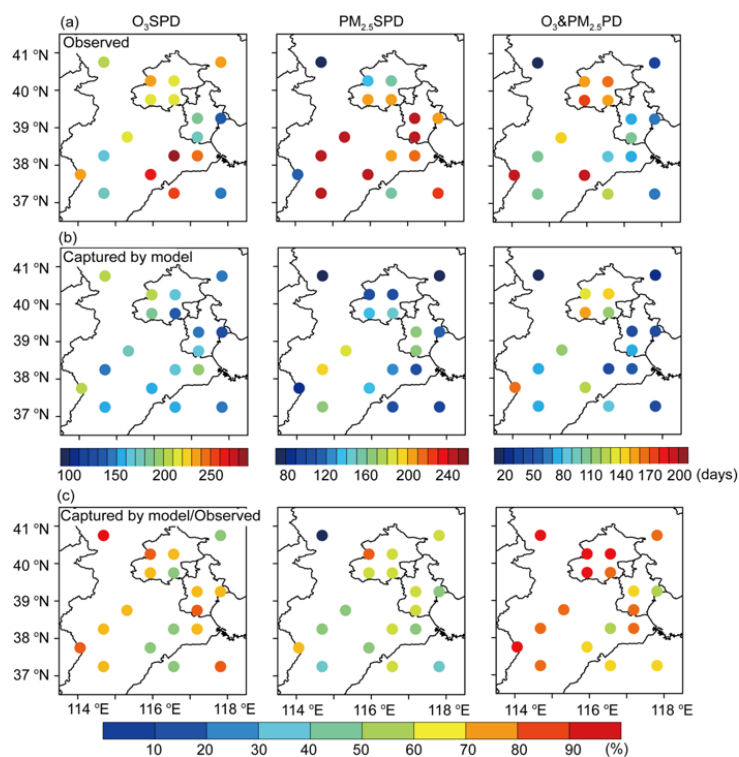
288 concentrations of air pollutants. Such deficiency was also reported in previous studies
289 that used the GEOS-Chem model or the weather Research and Forecasting with
290 Chemistry (WFR-chem) model (Zhang et al., 2016; Ni et al., 2018; Gong and Liao,
291 2019; Dang and Liao, 2019). Therefore, to identify O₃PD, PM_{2.5}PD, and O₃&PM_{2.5}PD
292 using model results, we utilized lower thresholds by considering the NMBs of simulated
293 MDA8 O₃ and PM_{2.5} concentrations in each of 18 grids of BTH. Taking the grid of
294 Beijing as an example, simulated MDA8 O₃ and PM_{2.5} had NMBs of -22.0% and -
295 26.9%, respectively, as the simulated concentrations were compared with observations
296 for days with observed concentrations higher than the national air quality standards over
297 the warm seasons of 2013-2020. We then adjusted the threshold of O₃PD in this grid to
298 be 62.4 ppb (80 ppb×78%) and that of PM_{2.5}PD to be 54.8 μg m⁻³ (75 μg m⁻³×73.1%).
299 These adjusted thresholds were also used to identify O₃&PM_{2.5}PD. Such approach was
300 also used in previous studies to better capture the pollution events based on the
301 simulations (Dang and Liao, 2019; Gong and Liao, 2019). With the adjusted thresholds,
302 56-93% of the observed O₃PD, PM_{2.5}PD, and O₃&PM_{2.5}PD can be captured by the
303 model (Fig. S2e).

304 **3.2.3 Simulated O₃SPD, PM_{2.5}SPD, and O₃&PM_{2.5}PD**

305 Since O₃PD or PM_{2.5}PD encompasses O₃&PM_{2.5}PD, we further define O₃ single
306 pollution days (hereafter called “O₃SPD”, which is to exclude O₃&PM_{2.5}PD from O₃PD)
307 and PM_{2.5} single pollution days (hereafter called “PM_{2.5}SPD”, which is to exclude
308 O₃&PM_{2.5}PD from PM_{2.5}PD) for the purpose of obtaining the characteristics of
309 different polluted days. Figures 4a and 4b show, respectively, the spatial distributions
310 of numbers of O₃SPD, PM_{2.5}SPD, and O₃&PM_{2.5}PD from observations and from the
311 GEOS-Chem model using the adjusted thresholds. Considering the total of polluted
312 days in 18 grids in BTH, observed O₃SPD, PM_{2.5}SPD, and O₃&PM_{2.5}PD were,



313 respectively, 3937, 3698, and 2024 days, in which 75.0% (2954/3937), 58.1%
314 (2148/3698), and 79.7% (1614/2024) were captured by observation and simulation
315 simultaneously (Fig. 4c). In addition, the numbers of observed and captured O₃SPD,
316 PM_{2.5}SPD, and O₃&PM_{2.5}PD in each month are shown in Fig. S3. The model has a
317 fairly good capability of capturing the observed polluted days in each month.



318
319 **Figure 4.** Spatial distributions of (a) observed numbers of O₃SPD, PM_{2.5}SPD, and
320 O₃&PM_{2.5}PD, (b) numbers of polluted days that were observed and also captured by
321 the GEOS-Chem model with adjusted thresholds, and (c) percentages of observed
322 polluted days that were captured by the model with adjusted thresholds. The values
323 were calculated for the warm months (April to October) of 2013-2020.

324

325 **3.3 Chemical characteristics of polluted days by O₃ and PM_{2.5}**



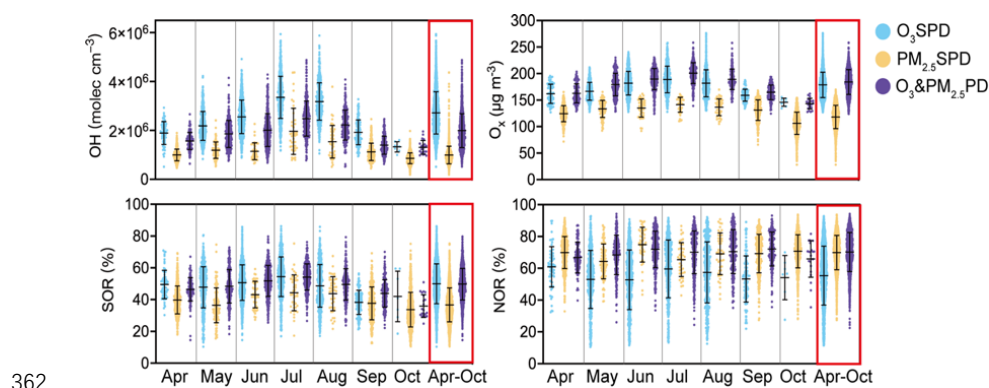
3.3.1 Atmospheric oxidants of O₃SPD, PM_{2.5}SPD, and O₃&PM_{2.5}PD

Figure 5 shows the boxplots of daily concentrations of hydroxyl radical (OH) and total oxidant ($O_x = O_3 + NO_2$) from the model for days of O₃SPD, PM_{2.5}SPD, and O₃&PM_{2.5}PD that were observed and also captured by the model (samples in Fig. 4b) in the warm seasons of 2013-2020 in 18 grids of BTH. The levels of OH and O_x characterize the atmospheric oxidation capacity, following Hu et al. (2020) and Chan et al. (2017). The concentrations of OH were the highest in O₃SPD, with an averaged value of 2.8×10^6 molec cm⁻³, followed by that in O₃&PM_{2.5}PD (2.0×10^6 molec cm⁻³) and in PM_{2.5}SPD (1.0×10^6 molec cm⁻³). Due to the lack of publicly accessible observations of OH in BTH, we compare the simulated OH concentrations with observations reported in the literature. The simulated OH concentrations agree closely with the observed values. In Wangdu of BTH, while the observed daily maximum OH concentrations in summer of 2014 were in the range of $5\text{--}15 \times 10^6$ molec cm⁻³ (Tan et al., 2016), the simulated OH concentrations in the same time period in this work were $3.7\text{--}9.5 \times 10^6$ molec cm⁻³. In Beijing in summer of 2017, the observed daily mean OH concentration was 5.8×10^6 molec cm⁻³ (Woodward et al., 2020) and our simulated value was 2.4×10^6 molec cm⁻³.

The mean values of O_x were, respectively, 178.7, 118.1, and 184.1 $\mu\text{g m}^{-3}$ in O₃SPD, PM_{2.5}SPD, and O₃&PM_{2.5}PD, indicating that the atmospheric oxidation capacity was strong in O₃&PM_{2.5}PD, which favored the production of secondary components of PM_{2.5}. Figure 5 also shows sulfur oxidation ratio (SOR, $n\text{-SO}_4^{2-} / (n\text{-SO}_4^{2-} + n\text{-SO}_2)$, where $n\text{-SO}_4^{2-}$ and $n\text{-SO}_2$ are the concentrations of SO_4^{2-} and SO_2 , respectively) and nitrogen oxidation ratio (NOR, $n\text{-NO}_3 / (n\text{-NO}_3 + n\text{-NO}_2)$, where $n\text{-NO}_3$ and $n\text{-NO}_2$ are the concentrations of NO_3 and NO_2 , respectively). SOR and NOR are measures of the conversion degrees of sulfur and nitrogen, respectively (Zhu et al.,



351 2019). In O₃SPD, PM_{2.5}SPD, and O₃&PM_{2.5}PD, the averaged values of SOR were
352 50.0%, 36.7%, and 49.7%, and those of NOR were 55.4%, 70.0%, and 70.2%,
353 respectively. The high SOR and NOR in O₃&PM_{2.5}PD indicated the strong formation
354 of SO₄²⁻ and NO₃ that were promoted by high atmospheric oxidation capacity. The
355 monthly variations of OH, O_x, and SOR were similar (Fig. 5), with the highest values
356 in summer, owing to the high temperature that promoted high concentrations of
357 oxidants and SOR. It is interesting that SOR and O_x values were higher in O₃&PM_{2.5}PD
358 than in O₃SPD or in PM_{2.5}SPD during May-August. Similarly, NOR values were higher
359 in O₃&PM_{2.5}PD than in O₃SPD or in PM_{2.5}SPD in May and July-September. Overall,
360 the O₃&PM_{2.5}PD occurred with high levels of atmospheric oxidants, SOR, and NOR,
361 leading to combined increases in O₃ and PM_{2.5} concentrations.

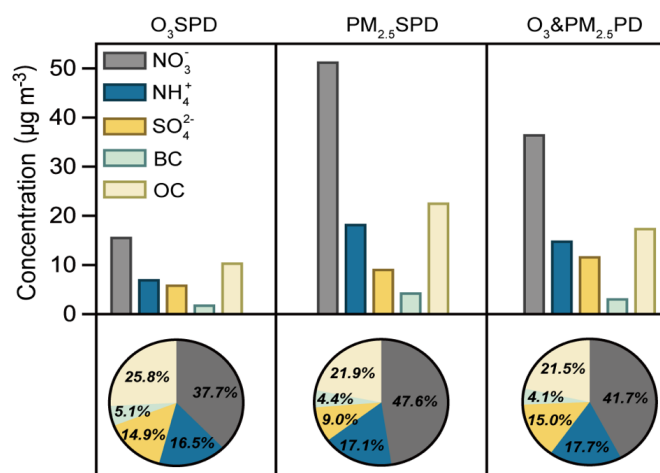


362
363 **Figure 5.** The boxplots of surface-layer hydroxyl radical (OH, molec cm⁻³), total
364 oxidant (O_x, μg m⁻³), sulfur oxidation ratio (SOR, %), nitrogen oxidation ratio
365 (NOR, %) for model-captured O₃SPD, PM_{2.5}SPD, and O₃&PM_{2.5}PD in 18 grids of
366 BTH in the months of April to October from 2013 to 2020. The whiskers represent the
367 standard deviation, the black line represents the mean value of the samples.

368 3.3.2 Surface-layer concentrations of PM_{2.5} components in O₃SPD, PM_{2.5}SPD, and 369 O₃&PM_{2.5}PD



370 The simulated concentrations of PM_{2.5} components (NO₃⁻, NH₄⁺, SO₄²⁻, BC, and
371 OC, averaged over 18 grids of BTH are shown in Fig. 6 for days of O₃SPD, PM_{2.5}SPD,
372 and O₃&PM_{2.5}PD in the warm seasons of 2013-2020 that were observed and also
373 captured by the model. While the mean concentrations of NO₃⁻, NH₄⁺, BC, and OC,
374 were all the highest in PM_{2.5}SPD, SO₄²⁻ concentration was the highest in O₃&PM_{2.5}PD.
375 In O₃SPD, PM_{2.5}SPD, and O₃&PM_{2.5}PD, the mean concentrations of SO₄²⁻ were 6.2,
376 9.4, and 11.97 μg m⁻³, respectively, and the percentages of SO₄²⁻ in PM_{2.5} were 14.9%,
377 9.0%, and 15.0%, respectively. In July and August, the concentrations of SO₄²⁻ and
378 MDA8 O₃ in O₃&PM_{2.5}PD were the highest compared with those in O₃SPD and
379 PM_{2.5}SPD (Fig. S4).



380

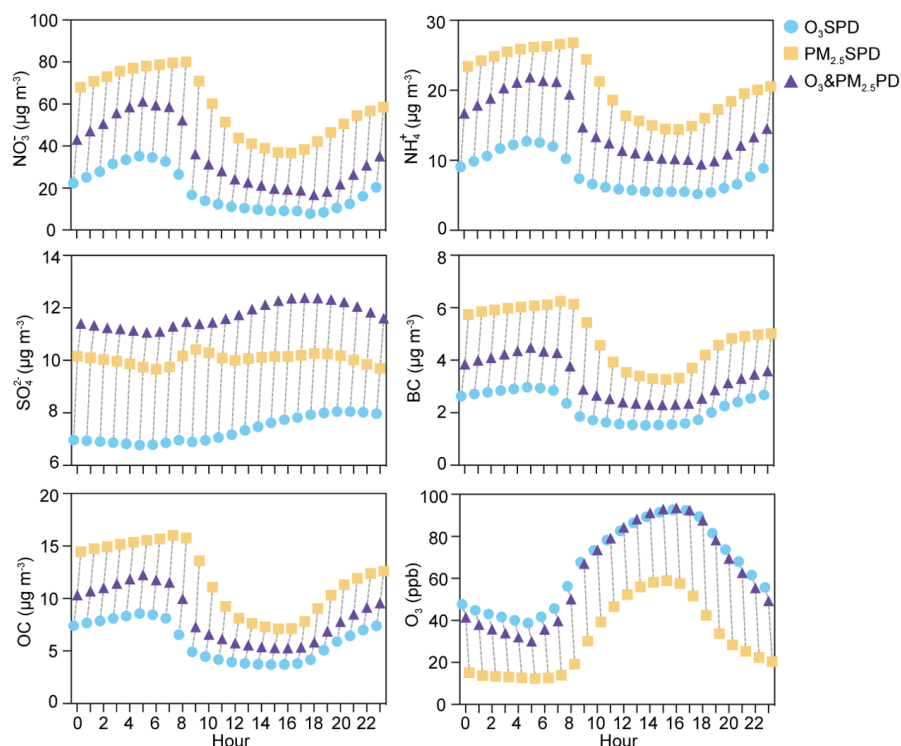
381 **Figure 6.** The concentrations of PM_{2.5} components (μg m⁻³) and percentages of PM_{2.5}
382 components (%) at the surface for NO₃⁻, NH₄⁺, SO₄²⁻, BC, and OC. The values were
383 averaged over the model-captured O₃SPD, PM_{2.5}SPD, and O₃&PM_{2.5}PD in the months
384 of April to October of 2013-2020 in BTH.

385 Figure 7 presents the hourly concentrations of NO₃⁻, NH₄⁺, SO₄²⁻, BC, OC, and O₃
386 for model-captured O₃SPD, PM_{2.5}SPD, and O₃&PM_{2.5}PD over all 18 grids of BTH in



387 the warm seasons from 2013-2020. Concentrations of NO_3^- and NH_4^+ had similarities
388 in diurnal variations, all of which reached the highest values in the early morning (5:00
389 local time (LT) in O_3SPD and $\text{O}_3\&\text{PM}_{2.5}\text{PD}$, 7:00-8:00 LT in $\text{PM}_{2.5}\text{SPD}$) and had the
390 lowest values in the late afternoon (18:00 LT in O_3SPD and $\text{O}_3\&\text{PM}_{2.5}\text{PD}$, 16:00 LT in
391 $\text{PM}_{2.5}\text{SPD}$). Concentrations of BC and OC peaked at the same time as those of NO_3^-
392 and NH_4^+ and had the lowest values at 15:00 LT in O_3SPD , $\text{PM}_{2.5}\text{SPD}$, and
393 $\text{O}_3\&\text{PM}_{2.5}\text{PD}$. The diurnal variations in NO_3^- , NH_4^+ , BC, OC reflected the diurnal
394 variations in PBLH (shown in Fig. S5), which generally reached their highest
395 concentrations before the sudden uplift of PBLH in the early morning (times for uplift
396 of PBLH: 6:00 LT in O_3SPD and $\text{O}_3\&\text{PM}_{2.5}\text{PD}$, 7:00 LT in $\text{PM}_{2.5}\text{SPD}$). Compared to
397 O_3SPD and $\text{O}_3\&\text{PM}_{2.5}\text{PD}$, the PBLH of $\text{PM}_{2.5}\text{SPD}$ was lower and uplifted one hour
398 later, which was more favorable for the accumulation of aerosols. During the daytime,
399 PBLH in $\text{O}_3\&\text{PM}_{2.5}\text{PD}$ was between O_3SPD and $\text{PM}_{2.5}\text{SPD}$.

400 It is worth noting that the diurnal variations of SO_4^{2-} were different from those of
401 other aerosol species, with the highest values at 20:00, 9:00, and 16:00 LT in O_3SPD ,
402 $\text{PM}_{2.5}\text{SPD}$, and $\text{O}_3\&\text{PM}_{2.5}\text{PD}$, respectively, and the lowest values in early morning and
403 night (5:00 LT in O_3SPD and $\text{O}_3\&\text{PM}_{2.5}\text{PD}$, 23:00 LT in $\text{PM}_{2.5}\text{SPD}$). For the diurnal
404 variation of O_3 , the highest values occurred during the daytime (16:00 LT in O_3SPD
405 and $\text{O}_3\&\text{PM}_{2.5}\text{PD}$, 15:00 LT in $\text{PM}_{2.5}\text{SPD}$) and the lowest values appeared at 5:00 LT
406 in all the cases. Therefore, in $\text{O}_3\&\text{PM}_{2.5}\text{PD}$, the time of the highest value of SO_4^{2-} was
407 the same as that of O_3 , indicating that SO_4^{2-} and O_3 were produced synergistically
408 during the daytime with strong atmospheric oxidation.



409

410 **Figure 7.** The hourly concentrations of NO_3^- , NH_4^+ , SO_4^{2-} , BC, OC, and O_3 averaged
411 over the model-captured O_3SPD , $\text{PM}_{2.5}\text{SPD}$, and O_3 & $\text{PM}_{2.5}\text{PD}$ in BTH in the months
412 of April to October of 2013-2020.

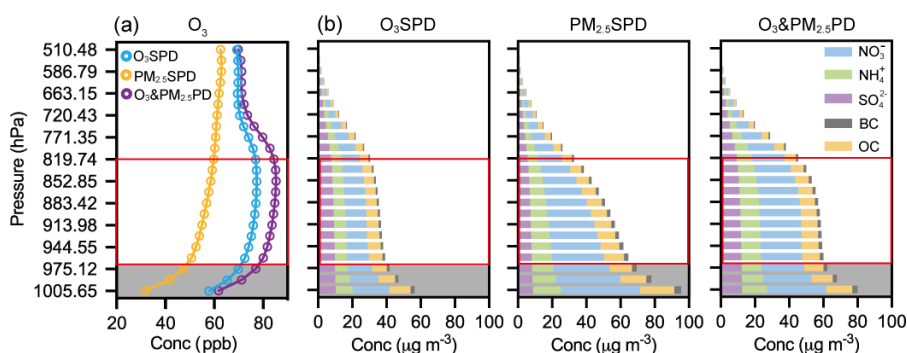
413 3.3.3 Vertical distributions of O_3 and $\text{PM}_{2.5}$ in O_3SPD , $\text{PM}_{2.5}\text{SPD}$, and 414 O_3 & $\text{PM}_{2.5}\text{PD}$

415 The simulated vertical distributions of O_3 and $\text{PM}_{2.5}$ averaged over the 18 grids of
416 BTH and the O_3SPD , $\text{PM}_{2.5}\text{SPD}$, and O_3 & $\text{PM}_{2.5}\text{PD}$ in warm seasons of 2013-2020 are
417 shown in Fig. 8. The vertical distribution of O_3 in O_3SPD was similar to that in
418 O_3 & $\text{PM}_{2.5}\text{PD}$ (Fig. 8a). In these two cases, concentrations of O_3 increased from the
419 surface to about 975 hPa, remained high between 975 and 819 hPa, and decreased with
420 altitude between 819 and 663 hPa. Although the magnitudes of O_3 were close at the
421 surface (61.9 ppbv in O_3 & $\text{PM}_{2.5}\text{PD}$ and 58.1 ppbv in O_3SPD), the concentration of O_3



422 averaged over 975 and 819 hPa was 10.4% higher in O₃&PM_{2.5}PD than in O₃SPD,
423 which was a very unique feature of O₃&PM_{2.5}PD. For the case of PM_{2.5}SPD, the
424 concentrations of O₃ were the lowest among the three cases and increased gently with
425 altitude above 975 hPa.

426 Figure 8b shows the vertical distributions of PM_{2.5} components. In all the cases,
427 PM_{2.5} concentrations were the highest at the surface, and decreased with altitude from
428 the surface to 975 hPa. However, concentrations of PM_{2.5} were quite stable between
429 975 and 819 hPa for O₃SPD (about 36.4 μg m⁻³) and O₃&PM_{2.5}PD (about 58.1 μg m⁻³),
430 corresponding to the stable O₃ levels at these altitudes in these two cases (Fig. 8a). For
431 PM_{2.5}SPD, while PM_{2.5} concentration at the surface was the highest among the three
432 cases, it decreased rapidly between 975 and 819 hPa. The averaged PM_{2.5} concentration
433 between 975 and 819 hPa was 52.4 μg m⁻³ in PM_{2.5}SPD, which was lower than that in
434 O₃&PM_{2.5}PD.



435
436 **Figure 8.** The vertical distributions of (a) concentrations of O₃ (ppb) and (b) PM_{2.5}
437 components (μg m⁻³) of NO₃⁻, NH₄⁺, SO₄²⁻, BC, OC averaged over the model-
438 captured O₃SPD, PM_{2.5}SPD, and O₃&PM_{2.5}PD in BTH in the months of April to
439 October of 2013-2020.

440 To further investigate the differences in vertical profiles of NO₃⁻, NH₄⁺, SO₄²⁻, BC,



441 OC, and PM_{2.5} in O₃SPD, PM_{2.5}SPD, and O₃&PM_{2.5}PD, the ratios of concentration at
 442 975 hPa to that at the surface as well as the concentration at 819 hPa to that at 975 hPa
 443 are shown in Table 1. The concentration of PM_{2.5} decreased largely, with the ratio of
 444 PM_{2.5}(975 hPa)/ PM_{2.5}(1005 hPa) of 0.78 in O₃&PM_{2.5}PD and of 0.74 in PM_{2.5}SPD. For each
 445 of the PM_{2.5} components, the ratios near the surface (from 1005 to 975 hPa, gray shaded
 446 area in Fig. 8) were close in the three types of pollution. While the ratios of NO₃⁻, NH₄⁺,
 447 BC, OC were in the range of 0.65-0.80, the ratios of SO₄²⁻ were about 0.93-0.98,
 448 indicating that SO₄²⁻ concentrations were quite uniform from the surface to 975 hPa in
 449 all three types of pollution.

450 **Table 1.** The ratios at 975 and 1005 hPa (gray shaded area in Fig. 8) and at 819 and
 451 975 hPa (red frame in Fig. 8) of NO₃⁻, NH₄⁺, SO₄²⁻, BC, OC, and PM_{2.5} in O₃SPD,
 452 PM_{2.5}SPD, and O₃&PM_{2.5}PD in BTH region.

		NO ₃ ⁻	NH ₄ ⁺	SO ₄ ²⁻	BC	OC	PM _{2.5}
Conc _{819 hPa} / Conc _{975 hPa}	O ₃ SPD	0.95	0.90	0.85	0.73	0.73	0.86
	PM _{2.5} SPD	0.64	0.68	0.81	0.64	0.63	0.67
	O ₃ &PM _{2.5} PD	0.94	0.91	0.87	0.79	0.77	0.89
Conc _{975 hPa} / Conc _{1005 hPa}	O ₃ SPD	0.65	0.77	0.96	0.69	0.70	0.74
	PM _{2.5} SPD	0.72	0.76	0.93	0.67	0.65	0.73
Conc _{1005 hPa}	O ₃ &PM _{2.5} PD	0.72	0.80	0.98	0.76	0.73	0.78

453
 454 In the upper layers (975-819 hPa, red rectangle in Fig. 8), the changes in
 455 concentrations of pollutants with altitude in PM_{2.5}SPD were quite different from those
 456 in O₃&PM_{2.5}PD and O₃SPD. The decline of PM_{2.5} from 975 to 819 hPa was slow in
 457 O₃&PM_{2.5}PD (PM_{2.5}(819 hPa)/PM_{2.5}(975 hPa)=0.89) and O₃SPD (0.86) and fast in PM_{2.5}SPD



458 (0.67). Considering that the variation of BC with altitude was mainly driven by
459 meteorology (Sun et al., 2020), the vertical variations of other components that differed
460 significantly from BC indicated the influences of chemical processes. In PM_{2.5}SPD,
461 NO₃⁻, NH₄⁺, OC had about the same ratio as BC (0.64) (with large decreases with
462 height), except for SO₄²⁻ concentration that had a ratio of 0.81. In O₃&PM_{2.5}PD, the
463 ratios of NO₃⁻, NH₄⁺, SO₄²⁻ were, 0.94, 0.91, 0.87, respectively, which were much
464 higher than the value of BC (0.79), indicating NO₃⁻, NH₄⁺, SO₄²⁻ were quite uniform
465 in the layers of 975-819 hPa with the influence of chemical processes, which will be
466 discussed further in Sect. 3.3.4 below.

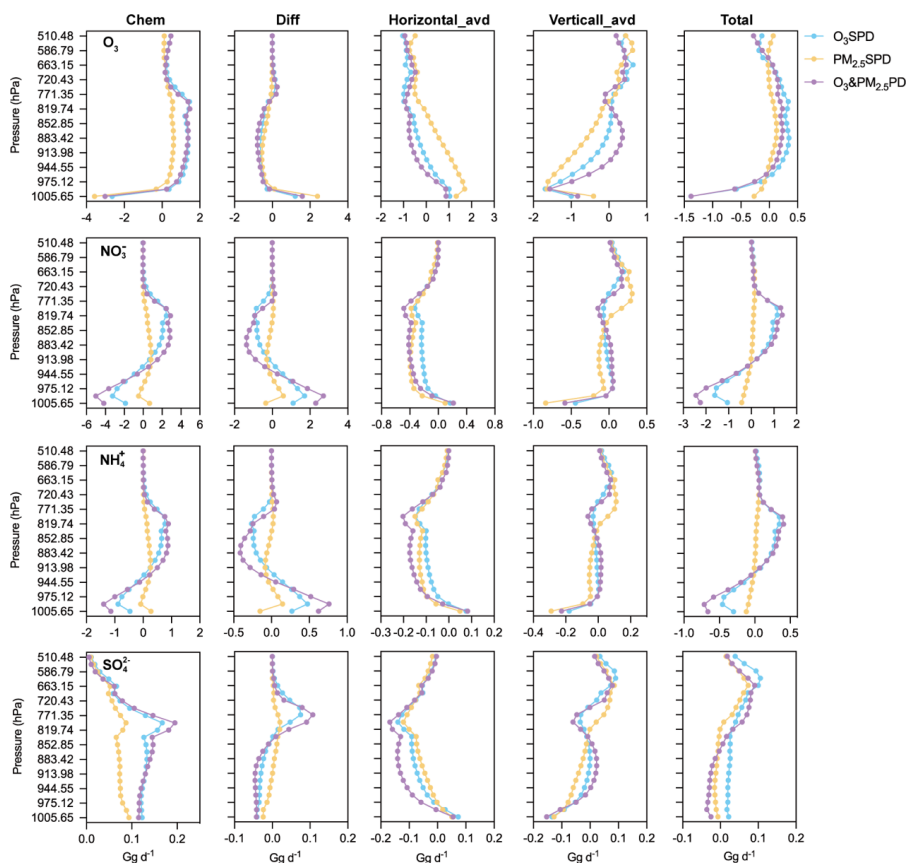
467 **3.3.4 Process analyses for O₃SPD, PM_{2.5}SPD, and O₃&PM_{2.5}PD**

468 The process analysis (PA) is applied to identify the relative importance of
469 atmospheric processes in the three types of pollution. Figure 9 shows the net changes
470 in O₃, NO₃⁻, NH₄⁺, SO₄²⁻ by the processes of chemical production (Chem), horizontal
471 advection (Horizontal_adv), vertical advection (Vertical_adv), and diffusion (Diff,
472 vertical PBL mixing process) in the GEOS-Chem model, as well as the total of all these
473 processes (i.e., Chem + Diff + Horizontal_adv + Vertical_adv) in O₃SPD, PM_{2.5}SPD,
474 and O₃&PM_{2.5}PD.

475 For O₃, the net changes of O₃ by all processes were positive at altitudes of 975-
476 819 hPa in O₃&PM_{2.5}PD and O₃SPD, in which Chem had the largest positive
477 contribution (about 1.5 Gg d⁻¹), indicating O₃ is chemically produced at these layers.
478 For NO₃⁻ and NH₄⁺, the nets of all processes increased mass concentrations at 913-819
479 hPa in O₃&PM_{2.5}PD and O₃SPD, in which Chem and Vertical_adv were positive and
480 Chem had the largest positive contribution. The vertical profiles of Chem were similar
481 for NO₃⁻ and NH₄⁺, both of which had the largest positive values at 913-819 hPa (2.83
482 Gg d⁻¹ for NO₃⁻ and 0.88 Gg d⁻¹ for NH₄⁺), leading to higher concentrations of NO₃⁻



483 and NH_4^+ in O_3 & $\text{PM}_{2.5}$ PD than in O_3 SPD and $\text{PM}_{2.5}$ SPD. For SO_4^{2-} , Chem was
484 positive from the surface to 510 hPa with a peak around 819 hPa, resulting in the
485 uniform SO_4^{2-} concentrations at these altitudes as shown in Fig. 8. Chem for SO_4^{2-} was
486 the highest around 819 hPa in O_3 & $\text{PM}_{2.5}$ PD, which was related to the strong liquid-
487 phase chemical formation of SO_4^{2-} (Fig. S6). In addition to Chem, Vertical_ave also
488 had positive contributions to the net changes in O_3 , NO_3^- , NH_4^+ , and SO_4^{2-} at 944-819
489 hPa. Vertical_ave was negative at 819 hPa and positive between 944 to 819 hPa,
490 implying that the pollutants were transported from 819 hPa to 944 hPa in O_3 & $\text{PM}_{2.5}$ PD.



491

492 **Figure 9.** The vertical profiles of net changes in O_3 , NO_3^- , NH_4^+ , and SO_4^{2-} (Gg d^{-1})

493 over BTH by each and total of processes. The values were averaged over the model-

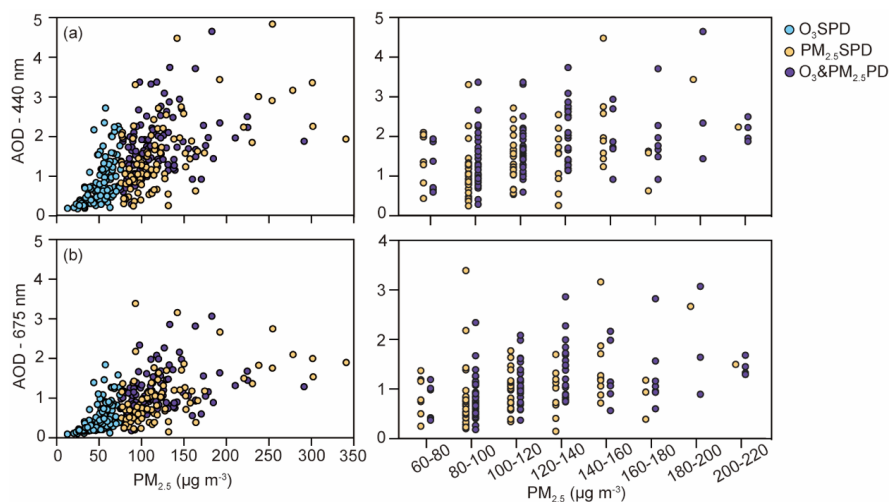


494 captured regional O₃SPD, PM_{2.5}SPD, and O₃&PM_{2.5}PD in April-October of 2013-
495 2020.

496 Overall, NO₃⁻, NH₄⁺, and SO₄²⁻ all had larger chemical productions at 913-819
497 hPa in O₃&PM_{2.5}PD compared to those in O₃SPD and PM_{2.5}SPD, accompanied by
498 strong vertical transport from 819 hPa to near the surface, resulting in the quite uniform
499 vertical profiles at 975-819 hPa in O₃&PM_{2.5}PD. In addition, the vertical profiles of net
500 changes in PM_{2.5} over BTH are shown in Fig. S7 for these three cases. Since NO₃⁻,
501 NH₄⁺, and SO₄²⁻ were the major components of PM_{2.5}, the PA of PM_{2.5} is similar to that
502 of each component.

503 3.3.5 Observed AOD in O₃SPD, PM_{2.5}SPD, and O₃&PM_{2.5}PD

504 To try to support the model result that O₃&PM_{2.5}PD had more uniform vertical
505 profile than PM_{2.5}SPD from the surface to 819 hPa altitude, we present the scatter plots
506 of observed AOD (at 440 nm and 675 nm) versus observed PM_{2.5} concentrations in
507 O₃SPD, PM_{2.5}SPD, and O₃&PM_{2.5}PD in Fig. 10. AERONET observations of AOD
508 from 2013 to 2020 are available at three sites in BTH (that is, Beijing (39.97°N, 116.38°
509 E), Beijing-CAMS (39.93°N, 116.31°E), Xianghe (39.75°N, 116.96°E)). At Beijing
510 (39.97°N, 116.38°E), AOD (440nm and 675nm) increased with PM_{2.5} concentration in
511 all three types of pollution. However, under the same levels of surface PM_{2.5}
512 concentration, AOD values in O₃&PM_{2.5}PD were higher than in PM_{2.5}SPD, implying
513 that the column burdens of aerosols were generally higher in O₃&PM_{2.5}PD than in
514 PM_{2.5}SPD, which may support the unique vertical distribution of PM_{2.5} in O₃&PM_{2.5}PD
515 shown in Fig. 8b. The scatter plots at Beijing-CAMS and Xianghe sites are similar and
516 are shown in Fig. S8.



517

518 **Figure 10.** The scatterplots of (a) AOD (440 nm) and (b) AOD (675 nm) versus
519 observed $\text{PM}_{2.5}$ concentrations in O_3SPD , $\text{PM}_{2.5}\text{SPD}$, and $\text{O}_3\&\text{PM}_{2.5}\text{PD}$ in Beijing
520 (39.97°N , 116.38°E) in April-October of 2013-2020.

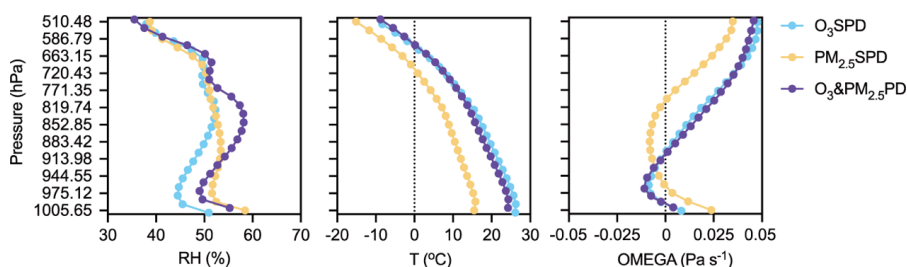
521

522 3.4 Meteorological conditions for O_3SPD , $\text{PM}_{2.5}\text{SPD}$, and $\text{O}_3\&\text{PM}_{2.5}\text{PD}$ over BTH

523 Figure 11 shows the vertical profiles of RH, T, and OMEGA for O_3SPD , $\text{PM}_{2.5}\text{SPD}$,
524 and $\text{O}_3\&\text{PM}_{2.5}\text{PD}$ captured by the model over BTH in the months of April to October
525 form 2013-2020. It should be noted that $\text{O}_3\&\text{PM}_{2.5}\text{PD}$ had an unique vertical
526 distribution of RH. Near the surface, the values of RH in $\text{O}_3\&\text{PM}_{2.5}\text{PD}$ were between
527 those in O_3SPD and $\text{PM}_{2.5}\text{SPD}$. However, in the upper layers (883-771 hPa),
528 $\text{O}_3\&\text{PM}_{2.5}\text{PD}$ had the highest RH among the three cases with a peak value of 58.2%.
529 As a result, the strongest aqueous chemical production of SO_4^{2-} (aqueous oxidation of
530 SO_2 by H_2O_2) occurred in $\text{O}_3\&\text{PM}_{2.5}\text{PD}$ around 819 to 771 hPa (Fig. S6). The vertical
531 profiles of temperature were similar in the three types of pollution, with the lowest
532 temperature in $\text{PM}_{2.5}\text{SPD}$. The vertical profiles of OMEGA were different in the three
533 cases. In O_3SPD and $\text{O}_3\&\text{PM}_{2.5}\text{PD}$, OMEGA had positive values around 819 hPa,



534 indicating a strong sinking airflow, leading to a downward transport of pollutants.
535 Under O₃&PM_{2.5}PD, the average values of PBLH and SWGDN were 946.1 m and
536 257.2 W m⁻², respectively, which were higher (lower) than those in PM_{2.5}SPD (O₃SPD)
537 (Fig. S9).

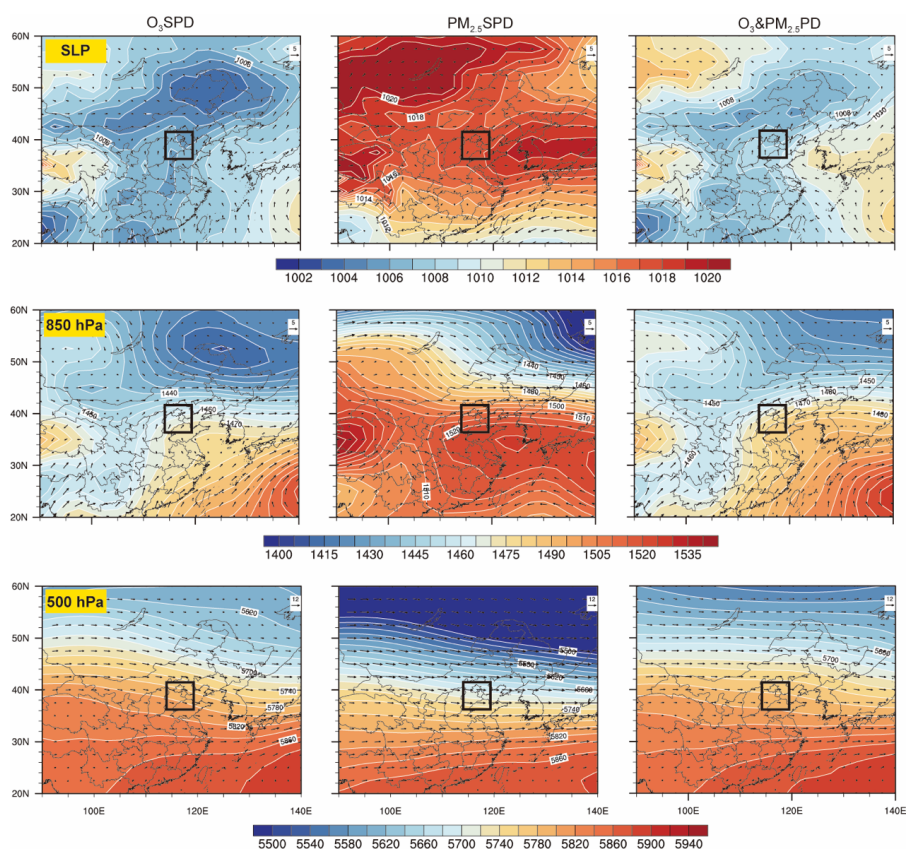


538
539 **Figure 11.** The vertical profiles of RH (%), T (°C), and OMEGA (Pa s⁻¹) averaged over
540 BTH and over the model-captured regional O₃SPD, PM_{2.5}SPD, and O₃&PM_{2.5}PD in in
541 April-October of 2013-2020.

542 Figure 12 shows the composited weather patterns for regional O₃SPD, PM_{2.5}SPD,
543 and O₃&PM_{2.5}PD (over 50% cities in the BTH experienced the pollution) that were
544 captured by the model in April-October of 2013-2020. The weather patterns of
545 O₃&PM_{2.5}PD were similar to some extent to those of O₃SPD but were quite different
546 from those of PM_{2.5}SPD. In O₃&PM_{2.5}PD, the BTH region was controlled by westerlies
547 at 500 hPa without cold air intrusion from the north, and was under the high pressure
548 ridge of the Western Pacific Subtropical High (WPSH) at 850 hPa. The strong
549 southerlies at 850 hPa brought moist air from the south (Fig. S10), resulting in a high
550 RH that was beneficial to the aqueous chemical production of SO₄²⁻ in O₃&PM_{2.5}PD.
551 In O₃SPD, BTH was also under the influence of the high pressure ridge of the WPSH
552 at 850 hPa, but it was weaker than in O₃&PM_{2.5}PD. Besides, the Northeast Cold Vortex
553 (NCV) was located to the southwest of BTH at 850 hPa in O₃SPD, leading to dry and
554 warm conditions, which was favorable for the formation of O₃. In PM_{2.5}SPD, the BTH
555 region was under the influence of both the continental high and the WPSH at 850 hPa.



556 At the surface, BTH was under the influence of a uniform high pressure with very weak
557 winds and hence stagnate atmosphere, which was conducive to the accumulation of
558 $PM_{2.5}$.



559
560 **Figure 12.** Composites of wind field ($m s^{-1}$) with SLP (sea level pressure) and with
561 geopotential height at 850 hPa and 500 hPa for regional O_3 SPD, $PM_{2.5}$ SPD, and
562 O_3 & $PM_{2.5}$ PD that were captured by the model in April-October of 2013-2020. The
563 solid black rectangle indicates BTH region.

564

565 4. Conclusions

566 We used the observed hourly concentrations of O_3 and $PM_{2.5}$ from CNEMC and
567 the model results from the nested-grid version of the GEOS-Chem model to examine



568 the chemical and physical characteristics of the co-polluted days by O₃ and PM_{2.5}
569 (O₃&PM_{2.5}PD) over the BTH region for eight warm seasons (April-October) from
570 2013 to 2020. The characteristic of O₃&PM_{2.5}PD were compared with those of the
571 polluted days by O₃ alone (O₃SPD) and by PM_{2.5} alone (PM_{2.5}SPD). In April-October
572 of 2013-2020, the observed O₃SPD, PM_{2.5}SPD, and O₃&PM_{2.5}PD were 2954, 2148,
573 and 1614 days, respectively, in which 75.0% (2954/3937), 58.1% (2148/3698), and
574 79.7% (1614/2024) were captured by the GEOS-Chem model, respectively. We
575 carried out composited analyses of the chemical and physical characteristics for
576 O₃SPD, PM_{2.5}SPD, and O₃&PM_{2.5}PD by using the samples (days) captured by both
577 the observations and the model.

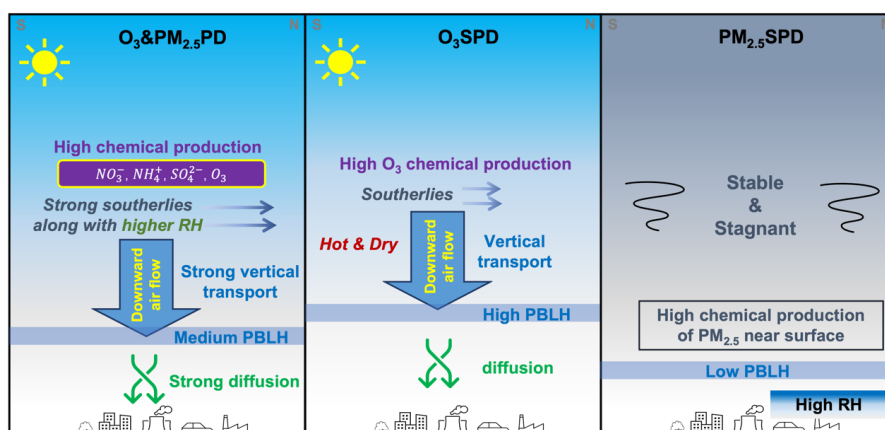
578 The chemical characteristics of O₃&PM_{2.5}PD were found to be different from
579 those of O₃SPD, PM_{2.5}SPD at the surface. O₃&PM_{2.5}PD occurred with high levels of
580 atmospheric oxidants (high OH and O_x), with higher SOR and NOR compared to those
581 in O₃SPD and PM_{2.5}SPD, leading to high concentrations of both O₃ and PM_{2.5}. At the
582 surface, the composited concentrations of NO₃⁻, NH₄⁺, BC, and OC were the highest in
583 PM_{2.5}SPD, while the composited concentration of SO₄²⁻ was the highest in
584 O₃&PM_{2.5}PD. There was a strong formation of SO₄²⁻ during the daytime in
585 O₃&PM_{2.5}PD in the oxidative atmosphere.

586 We also found unique features of the vertical distributions of O₃ and PM_{2.5} in
587 O₃&PM_{2.5}PD. Concentrations of PM_{2.5} were stable and high between 975 and 819 hPa
588 in O₃&PM_{2.5}PD, unlike those in PM_{2.5}SPD that decreased rapidly with the altitude. In
589 O₃&PM_{2.5}PD, the vertical profiles of NO₃⁻, NH₄⁺, and SO₄²⁻ were quite uniform at
590 975-819 hPa, corresponding to the stable O₃ concentrations at these altitudes. The
591 process analysis (PA) showed that NO₃⁻, NH₄⁺, and SO₄²⁻ all had larger chemical
592 productions at altitudes of 913-819 hPa in O₃&PM_{2.5}PD compared to those in O₃SPD



593 and $\text{PM}_{2.5}\text{SPD}$. The chemical production of SO_4^{2-} had large positive values from the
594 surface to about 500 hPa. The Vertical_avd also had positive contributions to the net
595 changes in O_3 , NO_3^- , NH_4^+ , and SO_4^{2-} at 944-819 hPa in $\text{O}_3\&\text{PM}_{2.5}\text{PD}$. Therefore, the
596 strong chemical productions at 913-819 hPa accompanied by the downward transport
597 resulted in the quite uniform vertical profiles at 975-819 hPa in $\text{O}_3\&\text{PM}_{2.5}\text{PD}$.

598 Figure 13 summarizes the chemical and physical characteristics in $\text{O}_3\&\text{PM}_{2.5}\text{PD}$,
599 O_3SPD , and $\text{PM}_{2.5}\text{SPD}$ in the BTH region. In $\text{O}_3\&\text{PM}_{2.5}\text{PD}$, the strong chemical
600 productions of O_3 , NO_3^- , NH_4^+ , and SO_4^{2-} occur at high altitudes of 913-819 hPa where
601 RH is high, and the accompanied downward airflow causes the stable concentrations at
602 944-819 hPa. The composited PBLH in $\text{O}_3\&\text{PM}_{2.5}\text{PD}$ is about 946.1 m, and the strong
603 mixed diffusion underneath the PBLH leads to high concentrations of pollutants at the
604 ground level. In contrast, O_3SPD occurs in hot and dry atmosphere with composited
605 PBLH of 1073.5 m. Strong O_3 chemical production occurs around 819 hPa, and O_3 is
606 then transported to the surface by downward air flow. The atmosphere is stable and
607 stagnate when $\text{PM}_{2.5}\text{SPD}$ occurs, with the lowest PBLH of 681.8 m. High RH (high
608 chemical formation of $\text{PM}_{2.5}$) and the accumulation of aerosols lead to the highest
609 surface-layer $\text{PM}_{2.5}$ in $\text{PM}_{2.5}\text{SPD}$.



610



611 **Figure 13.** A schematic diagram of chemical and physical and characteristics in
612 O₃SPD, PM_{2.5}SPD, and O₃&PM_{2.5}PD in BTH region.



613 ***Data availability.***

614 The GEOS-Chem model is available at <https://geos-chem.seas.harvard.edu> (last
615 access: 5 August 2022). The observed hourly surface concentrations of air pollutants
616 are derived from the China National Environmental Monitoring Center
617 (<https://air.cnemc.cn:18007/>, CNEMC, 2022). The simulation results are available
618 upon request from the corresponding author (hongliao@nuist.edu.cn).

619

620 ***Author contributions.***

621 HD and HL conceived the study and designed the experiments. HD performed model
622 simulations and analysed the data. KL, XY, YY, JZ, JJ, and BL provided useful
623 comments on the paper. HD and HL prepared the paper, with contributions from all co-
624 authors.

625

626 ***Competing interests.***

627 The authors declare that they have no conflict of interest.

628

629 ***Acknowledgements.***

630 We acknowledge the CNEMC for making their data publicly available. We
631 acknowledge the efforts of GEOS-Chem working groups for developing and
632 managing the model.

633

634 ***Financial support.***



635 This work was supported by the National Natural Science Foundation of China (Grant
636 No. 42021004) and the National Key Research and Development Program of China
637 (Grant No. 2019YFA0606800)



638 **References**

- 639 Alexander, B., Park, R. J., Jacob, D. J., Li, Q. B., Yan-
640 toska, R. M., Savarino, J., Lee,
641 C. C. W., and Thiemens, M. H.: Sulfate formation in sea-salt aerosols: Constraints
642 from oxygen isotopes, *J. Geophys. Res.-Atmos.*, 110, D10307,
643 <https://doi.org/10.1029/2004jd005659>, 2005.
- 644 Bey, I., Jacob, D. J., Yantosca, R. M., Logan, J. A., Field, B. D., Fiore, A. M., Li, Q. B.,
645 Liu, H. G. Y., Mickley, L. J., and Schultz, M. G.: Global modeling of tropospheric
646 chemistry with assimilated meteorology: Model description and evaluation, *J.*
647 *Geophys. Res.-Atmos.*, 106, 23073–23095, <https://doi.org/10.1029/2001jd000807>,
648 2001.
- 649 Chu, B. W., Ma, Q. X., Liu, J., Ma, J. Z., Zhang, P., Chen, T. A., Feng, Q. C., Wang. C.
650 Y., Yang, N., Ma, H. N., Ma, J. J., Russell, A. G., He, H.: Air Pollutant Correlations
651 in China: Secondary Air Pollutant Responses to NO_x and SO₂ Control, *Environ.*
652 *Sci. Tech. Let.*, 7(10), 695-700, <http://dx.doi.org/10.1021/acs.estlett.0c00403>,
653 2020.
- 654 Dai, H. B., Zhu, J., Liao, H., Li, J. D., Liang, M. X., Yang, Y., Yue, X.: Co-occurrence
655 of ozone and PM_{2.5} pollution in the Yangtze River Delta over 2013-2019:
656 spatiotemporal distribution and meteorological conditions, *Atmos. Res.*, 249,
657 105363, <https://doi.org/10.1016/j.atmosres.2020.105363>, 2021.
- 658 Dang, R. J. and Liao, H.: Severe winter haze days in the Beijing-Tianjin-Hebei region
659 from 1985-2017 and the roles of anthropogenic emissions and meteorology, *Atmos.*
Chem. Phys., 19, 10801-10816, <https://doi.org/10.5194/acp-19-10801-2019>, 2019.



- 660 Dang, R. J., Liao, H., and Fu, Y.: Quantifying the anthropogenic and meteorological
661 influences on summertime surface ozone in China over 2012-2017, *Sci. Total.*
662 *Environ.*, 754, 142394, <https://doi.org/10.1016/j.scitotenv.2020.142394>, 2021.
- 663 Fairlie, T. D., Jacob, D. J., and Park, R. J.: The impact of transpacific transport of
664 mineral dust in the United States, *Atmos. Environ.*, 41, 1251–1266,
665 <https://doi.org/10.1016/j.atmosenv.2006.09.048>, 2007.
- 666 Gao, Y. and Ji, H. B.: Microscopic morphology and seasonal variation of health effect
667 arising from heavy metals in PM_{2.5} and PM₁₀: One-year measurement in a densely
668 populated area of urban Beijing, *Atmos. Res.*, 212, 213–226, [https://doi.org/](https://doi.org/10.1016/j.atmosres.2018.04.027)
669 [10.1016/j.atmosres.2018.04.027](https://doi.org/10.1016/j.atmosres.2018.04.027), 2018.
- 670 Giles, D. M., Sinyuk, A., Sorokin, M. S., Schafer, J. S., Lyapustin, A.: Advancements
671 in the aerosol robotic network (aeronet) version 3 database – automated near real-
672 time quality control algorithm with improved cloud screening for sun photometer
673 aerosol optical depth (aod) measurements, *Atmos. Meas. Tech.*, 12, 169–209,
674 <https://doi.org/10.5194/amt-12-169-2019>. 2019.
- 675 Gonçalves, M., Jiménez-Guerrero, P., and Baldasano, J. M.: Contribution of
676 atmospheric processes affecting the dynamics of air pollution in South-Western
677 Europe during a typical summer-time photochemical episode, *Atmos. Chem. Phys.*,
678 9, 849–864, <https://doi.org/10.5194/acp-9-849-2009>, 2009.
- 679 Gong, C. and Liao, H.: A typical weather pattern for the ozone pollution events in North
680 China, *Atmos. Chem. Phys.*, 19, 13725-13740, [https://doi.org/10.5194/acp-19-](https://doi.org/10.5194/acp-19-13725-2019)
681 [13725-2019](https://doi.org/10.5194/acp-19-13725-2019), 2019.



- 682 Gong, C., Liao, H., Zhang, L., Yue, X., Dang, R. J., Yang, Y.: Persistent ozone pollution
683 episodes in North China exacerbated by regional transport, *Environ. Pollut.*, 265,
684 115056, <https://doi.org/10.1016/j.envpol.2020.115056>, 2020.
- 685 Guenther, A. B., Jiang, X., Heald, C. L., Sakulyanontvittaya, T., Duhl, T., Emmons, L.
686 K., and Wang, X.: The Model of Emissions of Gases and Aerosols from Nature
687 version 2.1 (MEGAN2.1): an extended and updated framework for modeling
688 biogenic emissions, *Geosci. Model Dev.*, 5, 1471–1492,
689 <https://doi.org/10.5194/gmd-5-1471-2012>, 2012.
- 690 Jiang, N., Li, L., Wang, S., Li, Q., Dong, Z., Duan, S., Zhang, R., Li, S.: Variation
691 tendency of pollution characterization, sources, and health risks of PM_{2.5}-bound
692 polycyclic aromatic hydrocarbons in an emerging megacity in China: based on
693 three-year data, *Atmos. Res.*, 217, 81–92, [https://doi.org/10.1016/j.](https://doi.org/10.1016/j.atmosres.2018.10.023)
694 [atmosres.2018.10.023](https://doi.org/10.1016/j.atmosres.2018.10.023), 2019.
- 695 Li, K., Jacob, D. J., Shen, L., Lu, X., Smedt, D. I., Liao, H.: Increases in surface ozone
696 pollution in China from 2013 to 2019: anthropogenic and meteorological
697 influences, *Atmos. Chem. Phys.*, 20, 11423–11433, [https://doi.org/10.5194/acp-](https://doi.org/10.5194/acp-20-11423-2020)
698 [20-11423-2020](https://doi.org/10.5194/acp-20-11423-2020), 2020.
- 699 Li, K., Jacob, D. J., Liao, H., Zhu, J., Shah, V., Shen, L., Bates, K., Zhang, Q., Zhai, S.
700 X.: A two-pollutant strategy for improving ozone and particulate air quality in
701 China, *Nat. Geosci.*, 12, 906–910, <https://doi.org/10.1038/s41561-019-0464-x>,
702 2019.
- 703 Li, M., Wang, L., Liu, J.: Exploring the regional pollution characteristics and



- 704 meteorological formation mechanism of PM_{2.5} in North China during 2013-2017,
705 Environ. Int., 134, 105283, <https://doi.org/10.1016/j.envint.2019.105283>, 2019.
- 706 Li, M., Zhang, Q., Kurokawa, J.-I., Woo, J.-H., He, K., Lu, Z., Ohara, T., Song, Y.,
707 Streets, D. G., Carmichael, G. R., Cheng, Y., Hong, C., Huo, H., Jiang, X., Kang,
708 S., Liu, F., Su, H., and Zheng, B.: MIX: a mosaic Asian anthropogenic emission
709 inventory under the international collaboration framework of the MICS-Asia and
710 HTAP, Atmos. Chem. Phys., 17, 935–963, [https://doi.org/10.5194/acp-17-935-](https://doi.org/10.5194/acp-17-935-2017)
711 2017, 2017.
- 712 Liu, Y. X., Zhao, Q. B., Hao, X., Zhao, J. R., Zhang, Y., Yang, X., Fu, Q. Y., Xu, X. Y.,
713 Wang, X. F., Huo, J. T., Chen, J. M.: Increasing surface ozone and enhanced
714 secondary organic carbon formation at a city junction site: An epitome of the
715 Yangtze River Delta, China (2014–2017), Environ. Pollut., 265, 0269-7491,
716 <https://doi.org/10.1016/j.envpol.2020.114847>, 2020.
- 717 Lou, S. J., Liao, H., Yang, Y., and Mu, Q.: Simulation of the interannual variations of
718 tropospheric ozone over China: Roles of variations in meteorological parameters
719 and anthropogenic emissions, Atmos. Environ., 122, 839–851,
720 <https://doi.org/10.1016/j.atmosenv.2015.08.081>, 2015.
- 721 Molod, A., Takacs, L., Suarez, M., and Bacmeister, J.: Development of the GEOS-5
722 atmospheric general circulation model: evolution from MERRA to MERRA2,
723 Geosci. Model Dev., 8, 1339–1356, <https://doi.org/10.5194/gmd-8-1339-2015>,
724 2015.
- 725 Mu, Q. and Liao, H.: Simulation of the interannual variations of aerosols in China:



- 726 role of variations in meteorological parameters, *Atmos. Chem. Phys.*, 14, 9597–
727 9612, <https://doi.org/10.5194/acp-14-9597-2014>, 2014.
- 728 Nan, J. L., Wang, S. S., Guo, Y. L., Xiang, Y. J., Zhou, B.: Study on the daytime OH
729 radical and implication for its relationship with fine particles over megacity of
730 Shanghai, China, *Atmos. Environ.*, 154, 167–178,
731 <https://doi.org/10.1016/j.atmosenv.2017.01.046>, 2017.
- 732 Ni, R., Lin, J., Yan, Y., and Lin, W.: Foreign and domestic contributions to springtime
733 ozone over China, *Atmos. Chem. Phys.*, 18, 11447–11469,
734 <https://doi.org/10.5194/acp-18-11447-2018>, 2018.
- 735 Park, R. J., Jacob, D. J., Chin, M., and Martin, R. V.: Sources of carbonaceous aerosols
736 over the United States and implications for natural visibility, *J. Geophys. Res.-*
737 *Atmos.*, 108, 4355, <https://doi.org/10.1029/2002jd003190>, 2003.
- 738 Park, R. J., Jacob, D. J., Field, B. D., Yantosca, R. M., and Chin, M.: Natural and
739 transboundary pollution influences on sulfate-nitrate-ammonium aerosols in the
740 United States: Implications for policy, *J. Geophys. Res.-Atmos.*, 109, D15204,
741 <https://doi.org/10.1029/2003jd004473>, 2004.
- 742 Pye, H. O. T., Liao, H., Wu, S., Mickley, L. J., Jacob, D. J., Henze, D. K., and Seinfeld,
743 J. H.: Effect of changes in climate and emissions on future sulfate-nitrate-
744 ammonium aerosol levels in the United States, *J. Geophys. Res.-Atmos.*, 114,
745 D01205, <https://doi.org/10.1029/2008jd010701>, 2009.
- 746 Qin, Y., Li, J. Y., Gong, K. J., Wu, Z., Chen, M. D., Qin, M. M., Huang, L., Hu, J. L.:
747 Double high pollution events in the Yangtze River Delta from 2015 to 2019:



- 748 Characteristics, trends, and meteorological situations, *Sci. Total. Environ.*, 792,
749 148349, <https://doi.org/10.1016/j.scitotenv.2021.148349>, 2021.
- 750 Ren, W., Tian, H., Tao, B., Chappelka, A., Sun, G., Lu, C., Liu, M., Chen, G., Xu, X.:
751 Impacts of tropospheric ozone and climate change on net primary productivity and
752 net carbon exchange of China's forest ecosystems, *Glob. Ecol. Biogeogr.*, 20, 391–
753 406, <https://doi.org/10.1111/j.1466-8238.2010.00606.x>, 2011.
- 754 Sun, T., Wu, C. and Wu, D.: Time-resolved black carbon aerosol vertical distribution
755 measurements using a 356-m meteorological tower in Shenzhen, *Theor. Appl.*
756 *Climatol.*, 140, 1263–1276, <https://doi.org/10.1007/s00704-020-03168-6>, 2020.
- 757 Tan, Z. F., Fuchs, H., and Lu, K. D.: Radical chemistry at a rural site (Wangdu) in the
758 North China Plain: Observation and model calculations of OH, HO₂ and RO₂
759 radicals, *Atmos. Chem. Phys.*, 17(1): 663–690, [https://doi.org/10.5194/acp-17-](https://doi.org/10.5194/acp-17-663-2017)
760 663-2017, 2017.
- 761 Wang, H., Kiang, C., Tang, X., Zhou, X., Chameides, W. L.: Surface ozone: a likely
762 threat to crops in Yangtze delta of China, *Atmos. Environ.*, 39, 3843–3850,
763 <https://doi.org/10.1016/j.atmosenv.2005.02.057>, 2005.
- 764 Wang, X., Manning, W., Feng, Z., Zhu, Y.: Ground-level ozone in China: distribution
765 and effects on crop yields, *Environ. Pollut.*, 147 (2), 394–400, [https://](https://doi.org/10.1016/j.envpol.2006.05.006)
766 doi.org/10.1016/j.envpol.2006.05.006, 2007.
- 767 Woodward-Massey, R., Slater, E. J., Alen, J.: Implementation of a chemical background
768 method for atmospheric OH measurements by laser-induced fluorescence:
769 characterisation and observations from the UK and China, *Atmos. Meas. Tech.*,



- 770 13(6): 3119–3146, <https://doi.org/10.5194/amt-13-3119-2020>, 2020.
- 771 Yue, X., Unger, N., Harper, K., Xia, X., Liao, H., Zhu, T., Xiao, J., Feng, Z., Li, J.:
- 772 Ozone and haze pollution weakens net primary productivity in China, *Atmos.*
- 773 *Chem. Phys.*, 17, 6073–6089, <https://doi.org/10.5194/acp-2016-1025>, 2017.
- 774 Zhang, Y. and Wang, Y.: Climate-driven ground-level ozone extreme in the fall over the
- 775 Southeast United States, *P. Natl. Acad. Sci. USA*, 113, 10025–10030,
- 776 <https://doi.org/10.1073/pnas.1602563113>, 2016.
- 777 Zheng, B., Tong, D., Li, M., Liu, F., Hong, C., Geng, G., Li, H., Li, X., Peng, L., Qi, J.,
- 778 Yan, L., Zhang, Y., Zhao, H., Zheng, Y., He, K., and Zhang, Q.: Trends in China’s
- 779 anthropogenic emissions since 2010 as the consequence of clean air actions,
- 780 *Atmos. Chem. Phys.*, 18, 14095–14111, [https://doi.org/10.5194/acp-18-14095-](https://doi.org/10.5194/acp-18-14095-2018)
- 781 2018, 2018.
- 782 Zheng, B., Zhang, Q., Geng, G., Chen, C., Shi, Q., Cui, M., Lei, Y., He, K.: Changes in
- 783 China’s anthropogenic emissions and air quality during the COVID-19 pandemic
- 784 in 2020, *Earth Syst. Sci. Data*, 13, 2895–2907, [https://doi.org/10.5194/essd-13-](https://doi.org/10.5194/essd-13-2895-2021)
- 785 2895-2021, 2021.
- 786 Zhu, J., Chen, L., Liao, H., Dang, R. J.: Correlations between $PM_{2.5}$ and ozone over
- 787 China and associated underlying reasons, *Atmosphere*, 10(7), 352,
- 788 <https://doi.org/10.3390/atmos10070352>, 2019.
- 789 Zong, L., Yang, Y., and Gao, M.: Large-scale synoptic drivers of co-occurring
- 790 summertime ozone and $PM_{2.5}$ pollution in eastern China, *Atmos. Chem. Phys.*, 11,
- 791 9105–9124, <https://doi.org/10.5194/acp-21-9105-2021>, 2021.